ADVANCED MATERIALS
www.advmat.de

Mobile Trions in Electrically Tunable 2D Hybrid Perovskites

*Jonas D. Ziegler, Yeongsu Cho, Sophia Terres, Matan Menahem, Takashi Taniguchi, Kenji Watanabe, Omer Yaffe, Timothy C. Berkelbach, and Alexey Chernikov**

2D hybrid perovskites are currently in the spotlight of material research for light-harvesting and -emitting applications. It remains extremely challenging, however, to externally control their optical response due to the difficulties of introducing electrical doping. Here, an approach of interfacing ultrathin sheets of perovskites with few-layer graphene and hexagonal boron nitride into gate-tunable, hybrid heterostructures, is demonstrated. It allows for bipolar, continuous tuning of light emission and absorption in 2D perovskites by electrically injecting carriers to densities as high as 10^{12} cm^{-2}. This reveals the emergence of both negatively and positively charged excitons, or trions, with binding energies up to 46 meV, among the highest measured for 2D systems. Trions are shown to dominate light emission and propagate with mobilities reaching 200 cm^2 V^{-1} s^{-1} at elevated temperatures. The findings introduce the physics of interacting mixtures of optical and electrical excitations to the broad family of 2D inorganic–organic nanostructures. The presented strategy to electrically control the optical response of 2D perovskites highlights it as a promising material platform toward electrically modulated light-emitters, externally guided charged exciton currents, and exciton transistors based on layered, hybrid semiconductors.

1. Introduction

A Ruddlesden–Popper perovskites are natural 2D semiconductors composed of nanometer-thin inorganic layers separated by organic barriers.[1–3] Combining the optical quality of inorganic quantum-wells with the flexibility of organic crystals, they emerged as promising platforms in material science across the fields of photovoltaics,[4,5] optoelectronics,[6] and photonics.[7] However, it has remained very difficult to electrically control the optical response in this class of hybrid 2D materials due to persistent challenges to introduce doping.[8] Consequently, both the emission and absorption of light in 2D perovskites are typically determined by charge-neutral electron–hole pairs, known as excitons.[9,10] The excitons are tightly bound due to quantum confinement and reduced dielectric screening from organic barrier layers.[11–14]

In contrast, when free charge carriers are present, an exciton can bind an additional electron or hole to form a three-particle trion state.[9] At elevated charge densities such quasiparticle can be also described as a Fermi polaron, which is an exciton dressed by the electron–hole pair excitations of the Fermi sea.[15,16] Originally demonstrated for inorganic semiconductors,[17,18] trions were shown to combine strong light–matter coupling of the excitons with an electrical charge of free carriers, motivating the crossover between optics and charge transport.[19–21] For organic and inorganic–organic hybrid materials such as perovskites, however, trions remained elusive despite predictions of exceptionally large binding

J. D. Ziegler, S. Terres, A. Chernikov
Institute of Applied Physics and Würzburg-Dresden Cluster of Excellence ct.qmat
TU Dresden, 01062 Dresden, Germany
E-mail: alexey.chernikov@tu-dresden.de

Y. Cho
Department of Chemistry
Columbia University, New York
New York 10027, USA

The ORCID identification number(s) for the author(s) of this article can be found under https://doi.org/10.1002/adma.202210221.

DOI: 10.1002/adma.202210221

M. Menahem, O. Yaffe
Department of Chemical and Biological Physics
Weizmann Institute of Science
Rehovot 76100, Israel

T. Taniguchi
International Center for Materials Nanoarchitectonics
National Institute for Materials Science
Tsukuba 305-0047, Japan

K. Watanabe
Research Center for Functional Materials
National Institute for Materials Science
Tsukuba 305-0047, Japan

T. C. Berkelbach
Center for Computational Quantum Physics
Flatiron Institute
New York 10010, USA

T. C. Berkelbach
Department of Chemistry
Columbia University
New York 10027, USA

energies.[22,23] Only recently they were considered in the context of intense optical pumping of nanocrystals[24–26] and invoked to explain quantum beating phenomena in bulk perovskites.[27]

Here, we employ few-layer graphene and insulating hexagonal boron nitride to create field-effect transistor-like heterostructures. This approach is commonly applied for inorganic layered semiconductors and is conceptually similar to the thin-film 2D perovskite transistor devices using silicon technology.[3] We adopt it to introduce high free carrier densities in ultrathin perovskite layers to demonstrate trion formation in hybrid 2D perovskites and study their properties. Due to the binding of an electrical charge to an exciton, trions could be useful for generating and steering currents of excitons using electric fields. The latter is otherwise very challenging, since excitons by themselves are charge neutral. In this context, both a high trion binding energy of 46 meV and a sizable trion mobility around 200 $cm^2\ V^{-1}\ s^{-1}$ at 50 K, that we determine, are already very encouraging. It motivates future development of optoelectronic devices based on controllable trion quasiparticles.

2. Results and Discussion

To overcome the main challenge of doping perovskite-type semiconductors,[8] we take advantage of the layered nature of 2D perovskites, integrating them into artificial van der Waals heterostructures, illustrated in **Figure 1**a. Using polymer-free pick-up, ultrathin layers of phenylethylammonium-lead-iodide (PEA_2PbI_4) are encapsulated between thin sheets of hBN insulators that ensure environmental protection[28,29] and serve as gate dielectrics. A few-layer graphene flake is added as a top gate and another one contacts the PEA_2PbI_4 layer directly. Both graphene flakes are connected by gold contacts. An optical microscopy image of one of the fabricated structures is presented in Figure 1b and the employed technique of layer-by-layer assembly is outlined in detail in Experimental Section and Section S1, Supporting Information.

Integrating 2D perovskites in such a field-effect device geometry allows us to electrically control the optical response by a continuous, in-situ tuning of free carrier densities. Photoluminescence (PL) signals measured on a typical device cooled

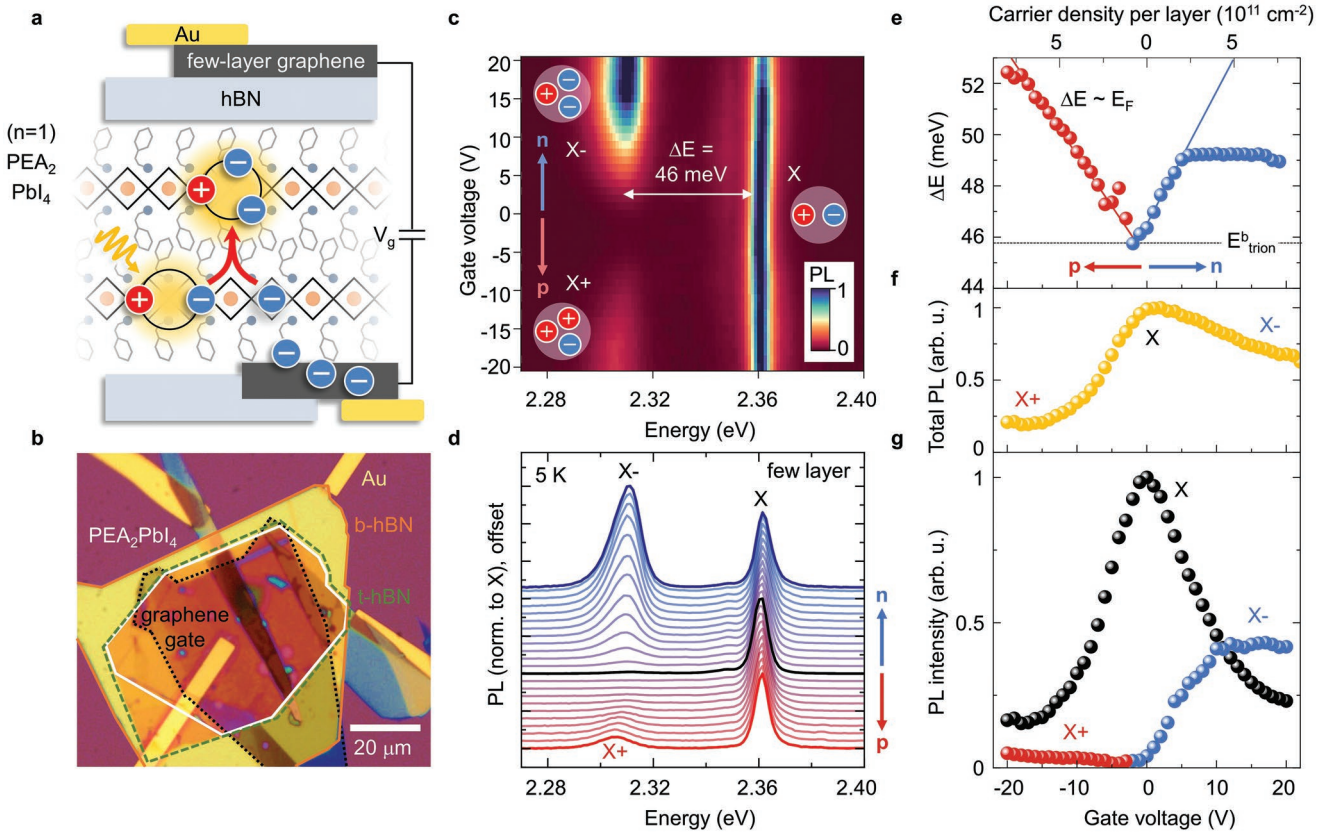

Figure 1. Charged excitons in electrically doped hybrid 2D perovskites. a) Illustration of an electrically gated, few-nm thin layer of a 2D hybrid perovskite ($n = 1$, PEA_2PbI_4), combined with few-layer graphene contacts and 10's of nm thin hBN as gate dielectric. b) Optical microscopy image of a typical device, assembled by mechanical exfoliation and re-stacking of the individual layers connected to prepatterned gold contacts. c) PL spectra in the range of the fundamental exciton transition, presented in a false-color plot as function of photon energy and gate voltage. Positively and negatively charged exciton states (trions) emerge at elevated gate voltages. d) Selected PL spectra across n- and p-doped regimes, normalized to the *X* peak intensity for each voltage (see Supporting Information for as-measured spectra). e) Energy difference between excitons and trions as function of gate voltage and estimated free carrier density per layer. The zero-voltage limit defines the trion binding energy of 46 meV. f) Total PL yield as function of gate voltage. g) Relative PL intensities of neutral exciton and negatively and positively charged trion states. All data was acquired at the temperature of 5 K under high-vacuum conditions.

down to 5 K are shown in Figure 1c as a function of photon energy and gate voltage. A number of selected spectra are presented in Figure 1d. At zero gate voltage, the PL is typical for high-quality PEA_2PbI_4[30] being dominated by a spectrally narrow, neutral exciton resonance (X) at 2.36 eV. For both positive and negative gate voltages, the spectra change substantially and a second, low-energy peak appears at 2.31 eV. The energy separation from the exciton peak increases linearly with gate voltage and is accompanied by a transfer of the PL intensity, as demonstrated in Figure 1e,g.

These observations are characteristic features of n- and p-trions (X_- and X_+),[31] further supported by typically asymmetric spectral lineshapes due to the electron recoil effect.[32] When either free electrons or holes are electrically injected, they bind to excitons via Coulomb forces leading to the emergence of a trion resonance and reducing the intensity of the neutral exciton peak. The energy difference ΔE between X and $X_\pm$ transitions in the zero-density limit determines the trion binding energy[33] and is as high as 46 meV for the studied sample. This value is more than an order of magnitude larger than those found in traditional quantum wells[32] and can substantially exceed even the trion binding energies of hBN-encapsulated, inorganic monolayer semiconductors[31,33] (e.g., almost factor of two higher compared to the p-trion in monolayer $MoSe_2$[34] and 30% higher compared to the n-trion in WSe_2[35]). At elevated gate voltages, ΔE is shown to increase linearly, being proportional to the Fermi energy of the free charges.[32,33] This allows for the estimation of the free carrier density per layer, which is in the range of 10^{11} to 10^{12} cm^{-2} for the applied voltages. In addition, while the PL yield decreases on the p-doped side, the total PL intensity is only weakly affected by n-doping. At sufficiently high doping densities, the X_- emission dominates even that of the neutral excitons.

The finding of robust n-type trions in 2D perovskites is particularly interesting, since the emergence of trions is often accompanied by a strongly quenched luminescence in nanostructures.[33] Moreover, we also observe that the exciton–trion energy separation seems to reach a plateau at a certain gate voltage in the n-doped case, corresponding to the estimated free electron density of several 10^{11} cm^{-2} per layer. While it could be connected to a process limiting the maximum density of free electrons per layer, the trion/exciton PL ratio still increases far beyond this point. We also note that the above observations of trions and the continuous tuning of the PL spectra by changing the gate voltage, are highly reproducible, being realized in six different device structures (see Section S2, Supporting Information, also regarding hysteresis and stability over time). In particular, a higher PL intensity of the n-trion in comparison to the p-trion is a consistent finding. Also, two of the devices were tunable only in the n-doping direction, which may be connected to other phenomena that may occur in the studied scenario, such as emergence of charged trap states or ion migration.[36]

An additional feature of the trions formed by bright excitons and free carriers is their appearance in absorption-type measurements indicating substantial light–matter coupling strength. The latter is partially transferred from the excitons and leads to modifications also of the absorption-type response. In order to detect these changes, we extend our study to perovskite layers of more than 10 nm thickness, which feature stronger absorption and reflectance signals. Similarly to ultrathin layers, they host light-emitting trions, as illustrated by the PL spectra shown in the upper panel of **Figure 2**a. In addition, measured reflectance contrast data, presented in the lower panel, shows a resonance at the same energy emerging at elevated gate voltages. The particular shape of the spectra is determined by interferences within the multilayer structure and polaritonic effects. To extract the associated changes of light–matter coupling strength for excitons and trions, we use a model dielectric function parametrized by multiple complex Lorentzians and apply a transfer-matrix approach to fit the reflectance spectra (see Section S3, Supporting Information). Two example simulated spectra for the lowest and highest gate voltage are shown in the lower panel of Figure 2a.

The extracted oscillator strengths for the excitons and trions are presented in Figure 2b, normalized to that of the exciton at the neutrality point. Here, we illustrate the p-doped case with comparable observations for the n-doped regime of a similar device shown in Supporting Information. The trion oscillator strength increases linearly with the gate voltage, proportional to the free carrier density, as expected in both trion and Fermi polaron models.[16,32] It represents a linearly increasing probability to absorb a photon by creating an exciton that simultaneously binds a proximate free charge carrier to form a trion. Concomitantly, it is accompanied by a decrease of the neutral exciton oscillator strength, as the formation of excitons becomes less likely. The oscillator strengths of the n-trions extracted from a different device are in good quantitative agreement with the analysis of the p-trion (see Section S3, Supporting Information). We note, however, that the total oscillator strength of the two peaks is not conserved, which can be attributed to additional screening and Pauli blocking effects leading to resonance quenching. Altogether, the observation of a finite and linearly increasing oscillator strength of the low-energy peak strongly supports its interpretation as a trion.

Interestingly, while the observations on the thicker layer are overall very similar to those from the ultrathin flake, the extracted trion binding energy of about 30 meV is substantially smaller. These differences in trion binding energies are directly related to the changes of the dielectric environment of the material.[13] For thicker samples, the Coulomb interaction is primarily screened by the proximate PbI_4 layers with comparatively high dielectric constant.[37] In contrast, the screening is reduced due to a lower dielectric constant of the organic barriers and hBN encapsulation for ultrathin mono- or few-layer samples. For quantitative analysis we calculate trion binding energies for a model system composed of interacting charges in a PbI_4 layer with varying dielectric surroundings. The two- and three-body Hamiltonian (for excitons and trions) is parameterized by effective masses from first-principles calculations[29] and the charges interact via a modified thin-film Coulomb potential to account for dielectric contrast between different layers[23] (see Experimental Section for additional details). We simulate sample thickness by tuning the dielectric constant of the PbI_4 layer surroundings ε_{ext} from 1 to 6 (in units of the vacuum permittivity ε_0). The calculated trion binding energies are presented in Figure 2c as a function of the exciton binding energy. Both binding energies increase with decreasing ε_{ext}. We observe that trion binding energies around 30 and 50 meV correlate well to exciton binding energies in the 300 to 500 meV range. Experimental values for the studied thin and thick PEA_2PbI_4 samples are presented for direct comparison. Here,

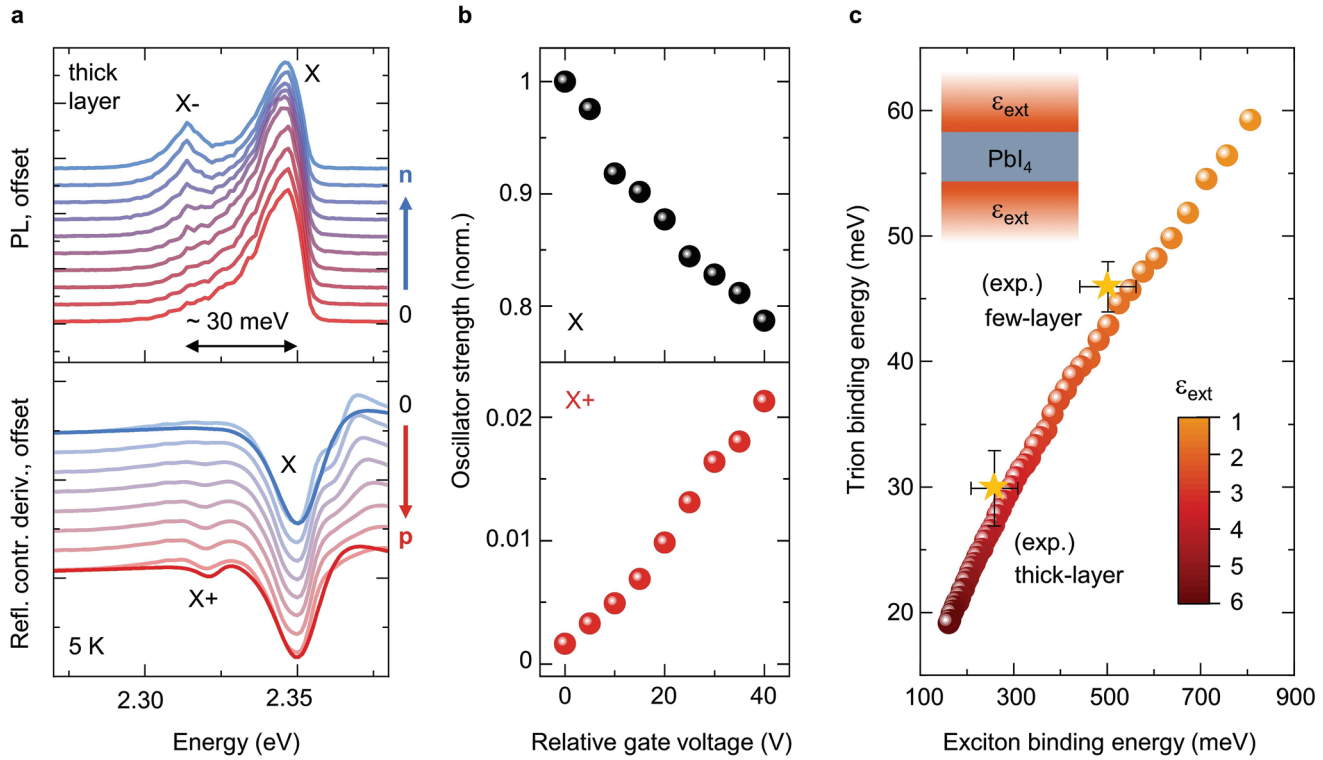

Figure 2. Trion binding energies and oscillator strengths. a) Top: Selected PL spectra for increasing free carrier densities obtained from an electrically gated device based on thick (>10 nm) 2D perovskite layer. Bottom: Reflectance contrast derivative spectra of the same device in the p-doped regime. b) Relative oscillator strengths of the excitons and trions extracted from reflectance contrast spectra, demonstrating partial transfer of the light-matter coupling strength. c) Trion and exciton binding energies calculated using a variational approach with modified thin-film Coulomb potential[23] for a series of environmental dielectric constants ε_{ext} surrounding the inorganic PbI_4 layer. Measured values of the trion and exciton binding energies from a few-nanometers thin and >10 nm-thick sample are indicated by stars.

the exciton binding energies are obtained by measuring excited exciton states 2s and 2p (in the hydrogen notation) using linear reflectance and two-photon photoluminescence excitation spectroscopy, respectively (see Section S3, Supporting Information).

Following the demonstration of electrically tunable trions in 2D perovskites, we now turn to their transport properties. In the context of exciton-carrier mixtures this is a particularly relevant aspect, since trion-like features can also be attributed to excitons bound to localized charged impurities (even if a sizable absorption would not be expected in that case). To monitor trion propagation, we first create local populations using tightly focused, 140 fs short optical pulses of a Ti:Sa laser and then detect the emitted PL as a function of both spatial and temporal coordinates using a streak camera (see Experimental Section). As schematically illustrated in **Figure 3**a, this allows us to directly monitor the diffusion of trions and measure their mobility. For these measurements we tune the gate voltage into the n-doped regime and use a spectral filter to detect only the trion emission during the first 200 ps. Corresponding PL transients of the excitons and trions are shown in the upper panel of Figure 3b. Interestingly, the trion lifetime is substantially longer than that of the neutral exciton. While it may be connected to the smaller oscillator strength of the trion compared to exciton and thus longer time-scales of the effective radiative recombination, it further highlights their stability combined with a high PL intensity of the n-type trions in particular.

To quantify trion transport, we extract the broadening σ of the spatial PL profiles at each time step after the excitation, according to a fit of the PL to the Gaussian form $\exp[-x^2/2\sigma(t)^2]$. Here, the spatial, 1D coordinate x is taken along the direction of the detected emission cross-section. The extracted variance $\sigma(t)^2$ corresponding to the PL emission area is presented in Figure 3b for a series of temperatures between 5 and 50 K. At the lowest temperatures we find no change of the trion spatial distribution with time, indicating localization. At higher temperatures of 35 and 50 K, however, we observe a linear increase of $\sigma(t)^2$, consistent with diffusive transport. From the relation $\Delta\sigma^2 = \sigma^2(t) - \sigma^2(0) = 2Dt$ we extract the diffusion coefficient D, presented in Figure 3c as a function of temperature. The data demonstrates thermally activated diffusion of the trions with a similar onset temperature of several tens of K as previously observed for neutral excitons in PEA_2PbI_4.[29] Therefore, the additional charge of trions does not alter the temperature-dependent localization behavior of neutral excitons. We could thus expect the trions to propagate freely also at higher temperatures, similar to the excitons. Most importantly, in contrast to hopping transport of tightly bound excitons in organic semiconductors,[38] the absolute diffusivity values are orders of magnitude higher and thus much closer to those in inorganic materials.[39,40] We determine the corresponding trion mobility using the relation $\mu_{eff} = eD/(k_BT)$ (e is the electron charge and k_B is the Boltzmann constant) and find it to be as high

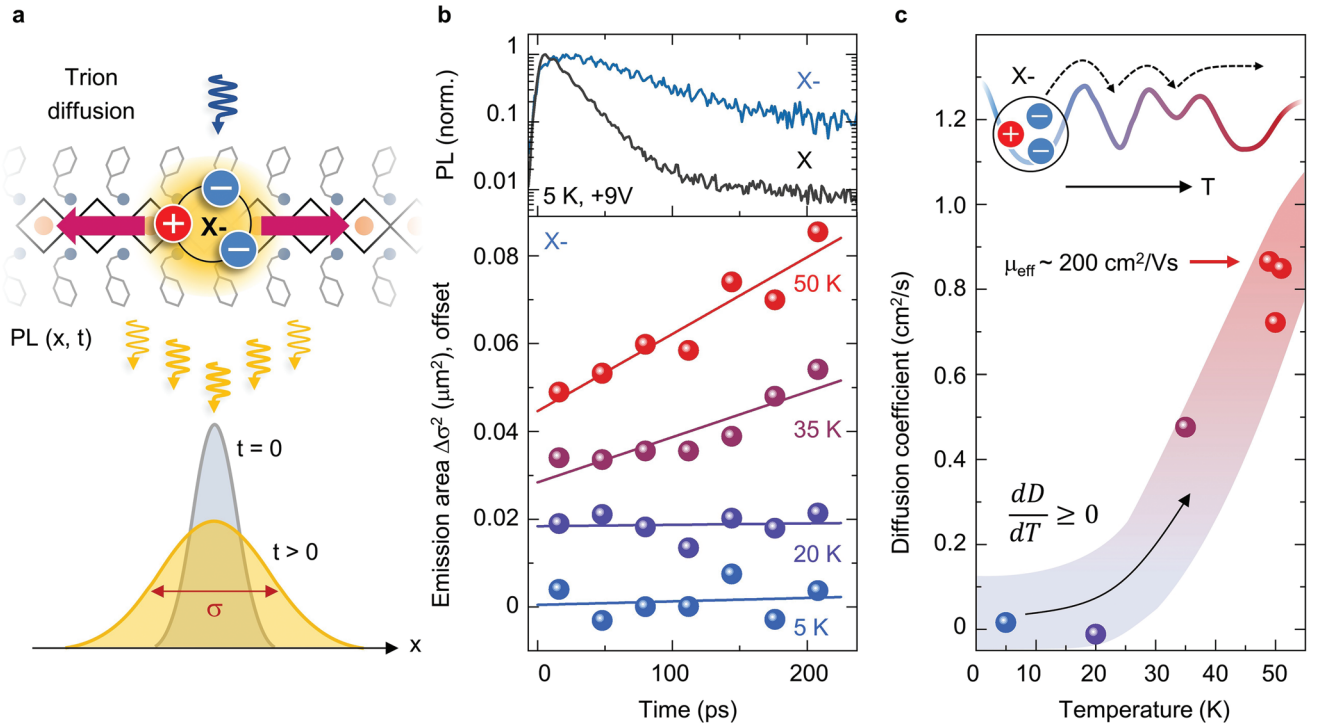

Figure 3. Spatially and time-resolved trion diffusion. a) Schematic illustration of the time- and spatially resolved measurements of trion diffusion. An ultrashort laser pulse creates trions in an electrically gated 2D perovskite. The emission of the propagating trion cloud is imaged and detected by a streak camera. b) Top: Transients of the exciton and trion PL demonstrating longer emission time of the trions. Bottom: Area of the trion PL as function of time for several temperatures between 5 and 50 K. Linear increase of the area with time signifies diffusive transport. c) Temperature dependent trion diffusion coefficient, revealing trion localization and thermally activated propagation (note that the values at 50 K are slightly displaced for better readability). The effective mobility of the trions obtained from $\mu_{eff} = eD/(k_BT)$ is on the order of 200 $cm^2\ V^{-1}\ s^{-1}$ at 50 K.

as 200 $cm^2\ V^{-1}\ s^{-1}$ for the diffusion coefficient of 0.85 $cm^2\ s^{-1}$ measured at 50 K.

3. Conclusion

The experimental demonstration of electrically tunable van der Waals heterostructures based on ultrathin 2D perovskites paves the way to electrically control the optical response of hybrid semiconductors. The emerging exciton-electron complexes combine electrical charge with strong light–matter coupling that should allow for guiding exciton currents and manipulating the optical response using external electric fields. Particularly remarkable and useful in this context is the observed combination of extremely high binding energies and substantial mobilities of the trions in 2D perovskites. Notably, the integration of hybrid and inorganic van der Waals materials should be easily transferable to a broad range of material combinations. This merges the chemical and structural flexibility of hybrid semiconducting nanostructures with the ability to simultaneously control electrical and optical excitations.

4. Experimental Section

Synthesis: PbO (99%), phosphinic acid (50% w in H_2O), 2-phenylethylamin (99%), and n-butylamine (99.5%), purchased from Merck, diethylether (BHT stabilized) purchased from Bio-Lab Chemicals and hydriodic acid (stabilizer free, 57% w in H_2O), purchased from Holland Moran were used. No additional treatment was employed on these reagents. The procedure reported in refs. [13] and [41] were used and adapted after refs. [42] and [43] to synthesize single crystals of phenyl-ethylammonium-lead-iodide, $(C_6H_5–CH_2CH_2NH_3)_2PbI_4$. In brief, PbO (0.3 g, 1.34 mmol) was dissolved in a mixture of hydriodic acid (1.3 mL, 10.2 mmol) and phosphinic acid (228 uL, 2 mmol) at 110 °C under magnetic stirring to a clear yellow solution. In a separated beaker placed in an ice-bath, 2-phenethylamine solution (171 µL, 1.34 mmol) was neutralized with hydriodic acid (11 mL, 83.5 mmol) and added to the PbI_2 solution, immediately leading to some precipitation. The magnetic stirring was continued until the solution was again of a clear yellow color. Hydriodic acid was added drop wise (about 1 mL) to speed up the dissolution. Then, the stirring was stopped, the beaker capped and cooled down to room temperature at a rate of 2 K h^{-1}. The orange plate-like crystals were further quenched in an ice bath, vacuum filtered, washed with diethylether, and dried at 90 °C in a vacuum oven for 24 h prior to use.

Gated Structure Fabrication: To prepare gate-controlled multilayer structures, micro-mechanical exfoliation of single crystals and two different polymer-assisted transfer methods were employed: the PDMS assisted stamping along ref. [44] and a modified version of the pick-up method outlined in ref. [45], further described in Section S1, Supporting Information. The structures were built from the synthesized PEA_2PbI_4 single crystals, high-quality hexagonal boron nitride (from NIMS, Japan) and commercially available graphite (from "HQgraphene") for few-layer graphene (FLG) contacts and gates. For both methods, the supporting structure consisting of hBN bottom layer, FLG contacts or bottom gates were prepared in the same way. Here, bulk crystals of hBN and graphite were thinned down between two sheets of Scotch tape and

transferred to blue backgrinding tape (Nitto). The blue tape was then carefully placed on a poly(dimethylsiloxane) (PDMS, Gel-Pak) stamp and removed, leaving few-layer flakes on the PDMS. The obtained flakes on PDMS were aligned under a microscope and subsequently stamped onto SiO_2/Si substrates with prepatterned gold contacts (5 nm Ti and 100 nm Au). The thickness of hBN layers was roughly chosen to be ≈20 to 30 nm to result in sufficiently high break-through voltages.

For the few-layer ultrathin samples assembled by the pick-up method, first a PDMS stamp was created by a drop of PDMS mixture (Dowsil) cured at 150 °C to obtain a round shape. A thin polypropylene-carbonate (PPC) layer was fabricated by dropping a few drops of PPC-solution (15% PPC in anisole) between two glass slides that were sled apart. Using a piece of Scotch tape with a small opening, the PPC layer was transferred on top of a PDMS stamp.

In parallel, SiO_2/Si substrates were cleaned first in a high-intensity ultrasonic bath in acetone and subsequently isopropyl alcohol as well as blow dried afterward. Remaining organic residues were removed by using oxygen plasma (at 200 W) for 5 min. Thin layers of hBN were directly exfoliated by bringing a blue tape loaded with crystals directly in contact with the SiO_2/Si substrate at a temperature of 100 °C, immediately followed by cooling it down and removing the tape. Then, using a temperature of 40 °C (around the glass transition temperature of PPC of 40 °C) the hBN was picked up by bringing the PPC-coated PDMS stamp in contact and slowly removing it again. Single crystals of PEA_2PbI_4 were thinned down by two sheets of Scotch tape and loaded on a backgrinding blue tape (Nitto). The direct exfoliation of perovskites was done similarly to hBN, but at a temperature of 50 °C that was used to achieve a high yield of PEA_2PbI_4 ultrathin layers. Immediately after the exfoliation, the ultrathin perovskite layer was picked up by the hBN on the PPC-PDMS stamp. The stack was then dropped onto the previously stamped hBN structure with graphene contacts and gate at a temperature of 50 °C.

Thicker perovskite layers were fabricated by using single crystals thinned down by Scotch tape and subsequently exfoliated on PDMS, similarly to hBN or FLG. Flakes with a thickness roughly between 10 and 40 nm were stamped across the few-layer graphene contacts and immediately covered with an additional hBN layer. An additional top gate was exfoliated using PDMS and stamped on top. The complete devices were finally contacted using an aluminum wire-bonder. The main advantage of the PDMS-stamping method was the simplicity of exfoliating all layers with the same method and subsequently stamping them layer-by-layer. However, ultrathin layers could not be reliably exfoliated on PDMS with sufficiently large sizes to be contacted. Therefore, the direct exfoliation on SiO_2/Si was used for creating the thinnest layers, followed by the more complex pick-up method described above.

Optical Spectroscopy: All measurements were conducted with the samples mounted inside a helium-flow cryostat (Cryovac) under high vacuum conditions. For the gate-dependent measurements, a custom-built breakout box connects the chip carrier inside the cryostat with a source-measure-unit (Keithley) to control the voltage. For the time-integrated PL measurements a continuous wave solid-state laser was used at a wavelength of 473 nm and a power of 5 nW. The laser was focused onto the sample by a glass-corrected 60× objective (Nikon), resulting in a spot size of ≈1 µm. The photoluminescence emission was filtered by tunable longpass filters (Semrock). For the reflectance contrast measurements a broadband tungsten halogen lamp (Newport) was used, focused by the same 60× objective to a spot size of about 1.5 µm. For the voltage-dependent measurements, the broadband spectrum of the lamp was spectrally filtered to the region of interest between 500 and 600 nm by a spectral filter, in order to keep the overall excitation power low. Both PL and reflectance signals were dispersed by a grating spectrometer and detected using a Peltier-cooled charge-coupled device (Roper Scientific).

For spatially and time-resolved measurements, the 140 fs pulses of a 80 MHz tunable Ti:Sa laser (Coherent) operating at 880 nm were frequency doubled by a SHG crystal (APE) and focused on the sample by the 60× objective to a spot size of ≈1 µm. The excitation density for the time-resolved measurements was kept below 16 nJ cm^{-2} to prevent light-induced degradation. The emission was filtered by a spectral filter and a mirror was used to directly image the cross-section onto a streak camera detector (Hamamatsu) providing temporal resolution. The streak camera was operated in the photon-counting mode. For the time- and spectrally-resolved measurements, a 300 mm^{-1} grating was used instead of a mirror to guide the light onto the streak camera. In this experiment, the laser pulse initially created a local population of excitons in the sample. Its distribution typically matched the shape of the excitation light focused by the objective. The excitons then diffused over time and a fraction of them emitted photons. Consequently, the area from which those photons were emitted also increased over time. In the linear density regime, at sufficiently low densities, this area represented the spread of the exciton population. To monitor it, the cross-section of the PL was imaged onto a streak camera detector. The streak camera then provided spatially resolved PL profiles at different times after the excitation. In the final image, the spatially and time-resolved intensity $I_{PL}(x,t)$ was detected as function of x on the horizontal axis and as function of t on the vertical axis. Whenever necessary the emission was spectrally filtered prior to detection. In case of strong PL signals, the intensity was reduced by neutral-density filters to avoid double-counting in the single-photon detection mode of the streak camera. The analysis of this type of data is outlined below.

Experimental Data Analysis: The emission spectra were corrected for the background, by subtracting acquired data with the light source turned off. In order to accurately determine the PL energy and intensity of each resonance, the neutral exciton was fitted using a symmetric Voigt profile. The trion resonance was fitted by a convolution of an exponential function for the low-energy flank with a Voigt profile. This lineshape accounted both for the electron recoil effect and symmetric broadening due to dephasing and inhomogeneities (see Section S3, Supporting Information). In some cases an additional weak, broadband emission at lower energies was subtracted.

The reflectance contrast is defined by $((R_{ref} - R)/(R_{ref} - R_{BG})$, where the reference spectrum R_{ref} is acquired on the bare substrate and R_{BG} corresponds to the background without illumination. The data was then analyzed using a transfer matrix approach to account for multilayer interference effects. The underlying stack was modeled using dielectric functions of each respective material from literature. Here, the dielectric function of the perovskite was parametrized by a background constant and two complex Lorentzians representing excitons and trions, respectively. The parameters of the two resonances and the thickness of the individual layers of the heterostructure were adjusted for the resulting reflectance contrast to match the experimental data. This procedure allowed for a quantitative extraction of the oscillator strength, peak position, and linewidth broadening by accounting for multilayer interferences. It also provided the effective absorption spectrum of the structure from reflectance contrast data in the spectra region of the exciton and trion resonances.

Binding Energy Calculations: The 2D exciton and trion Hamiltonians were defined in the effective mass approximation

$$H = -\sum_i \frac{\hbar^2 \nabla_i^2}{2m_i} + \sum_{i<j} q_i q_j W(r_{ij}) \quad (1)$$

where q_i are the charges of the particles. The effective masses m_i of the electron and hole were 0.19 and 0.25, respectively (in units of the electron mass), and they were assumed to be the same in the thick-layer and few-layer sample. These values were taken from the previous DFT calculations of the bulk PEA_2PbI_4 using the PBE functional and including spin-orbit coupling.[29,46] The Coulomb interaction W was calculated by modeling the PbI_4 layer as a uniform slab with dielectric constant 6.1[37] and thickness 6.3 Å surrounded by a uniform medium with dielectric constant ε_{ext}. The corresponding electrostatic problem was solved using the image charge method.[11]

The binding energy of the exciton and trion were calculated via approximate ground-state energies of the above Hamiltonian. The exciton binding energy is the ground-state energy of the exciton

Hamiltonian, and the trion binding energy is the difference between the ground-state energies of the trion and exciton Hamiltonians. For the exciton problem, the radial Schrodinger equation for the relative separation of the electron and hole was solved numerically on a real-space grid. For the trion problem, a variational wavefunction given by a linear combination of explicitly correlated Gaussian functions was used.[47] Additional functions were added via the stochastic variational method[23,48] until the energy converged to within 1 meV, which required about 50 to 70 explicitly correlated Gaussians.

Supporting Information

Supporting Information is available from the Wiley Online Library or from the author.

Acknowledgements

Financial support by the DFG via SPP2196 Priority Program (Project-ID: 424709454) and Emmy Noether Initiative (CH 1672/1, Project-ID: 287022282) as well as the Würzburg-Dresden Cluster of Excellence on Complexity and Topology in Quantum Matter ct.qmat (EXC 2147, Project-ID 390858490) is gratefully acknowledged. K.W. and T.T. acknowledge support from JSPS KAKENHI (Grant Numbers 19H05790, 20H00354, and 21H05233) Y.C. and T.C.B. acknowledge support from the US Air Force Office of Scientific Research under AFOSR Grant No. FA9550-19-1-0405. The Flatiron Institute is a division of the Simons Foundation.

Open access funding enabled and organized by Projekt DEAL.

Conflict of Interest

The authors declare no conflict of interest.

Data Availability Statement

The data that support the findings of this study are available from the corresponding author upon reasonable request.

Keywords

2D perovskites, diffusion, excitons, hybrid heterostructures, trions

Received: November 4, 2022
Revised: January 27, 2023
Published online: March 21, 2023

[1] T. Ishihara, J. Takahashi, T. Goto, *Solid State Commun.* **1989**, *69*, 933.
[2] D. B. Mitzi, C. A. Feild, W. T. A. Harrison, A. M. Guloy, *Nature* **1994**, *369*, 467.
[3] C. R. Kagan, D. B. Mitzi, C. D. Dimitrakopoulos, *Science* **1999**, *286*, 945.
[4] H. Tsai, W. Nie, J.-C. Blancon, C. C. Stoumpos, R. Asadpour, B. Harutyunyan, A. J. Neukirch, R. Verduzco, J. J. Crochet, S. Tretiak, L. Pedesseau, J. Even, M. A. Alam, G. Gupta, J. Lou, P. M. Ajayan, M. J. Bedzyk, M. G. Kanatzidis, A. D. Mohite, *Nature* **2016**, *536*, 312.
[5] C. Liang, H. Gu, Y. Xia, Z. Wang, X. Liu, J. Xia, S. Zuo, Y. Hu, X. Gao, W. Hui, L. Chao, T. Niu, M. Fang, H. Lu, H. Dong, H. Yu, S. Chen, X. Ran, L. Song, B. Li, J. Zhang, Y. Peng, G. Shao, J. Wang, Y. Chen, G. Xing, W. Huang, *Nat. Energy* **2021**, *6*, 38.
[6] Y. Chen, Y. Sun, J. Peng, J. Tang, K. Zheng, Z. Liang, *Adv. Mater.* **2018**, *30*, 1703487.
[7] N. Wang, L. Cheng, R. Ge, S. Zhang, Y. Miao, W. Zou, C. Yi, Y. Sun, Y. Cao, R. Yang, Y. Wei, Q. Guo, Y. Ke, M. Yu, Y. Jin, Y. Liu, Q. Ding, D. Di, L. Yang, G. Xing, H. Tian, C. Jin, F. Gao, R. H. Friend, J. Wang, W. Huang, *Nat. Photonics* **2016**, *10*, 699.
[8] J. Euvrard, Y. Yan, D. B. Mitzi, *Nat. Rev. Mater.* **2021**, *6*, 531.
[9] C. Klingshirn, *Semiconductor Optics*, 3rd Edition, Springer, Berlin/Heidelberg, Germany **2007**.
[10] H. Haug, S. W. Koch, *Quantum Theory of the Optical and Electronic Properties of Semiconductors*, 5th Edn., World Scientific, Singapore **2009**.
[11] K. Tanaka, T. Takahashi, T. Kondo, T. Umebayashi, K. Asai, K. Ema, *Phys. Rev. B* **2005**, *71*, 045312.
[12] K. Gauthron, J.-S. Lauret, L. Doyennette, G. Lanty, A. Al Choueiry, S. J. Zhang, A. Brehier, L. Largeau, O. Mauguin, J. Bloch, E. Deleporte, *Opt. Express* **2010**, *18*, 5912.
[13] O. Yaffe, A. Chernikov, Z. M. Norman, Y. Zhong, A. Velauthapillai, A. van der Zande, J. S. Owen, T. F. Heinz, *Phys. Rev. B* **2015**, *92*, 045414.
[14] J.-C. Blancon, A. V. Stier, H. Tsai, W. Nie, C. C. Stoumpos, B. Traoré, L. Pedesseau, M. Kepenekian, F. Katsutani, G. T. Noe, J. Kono, S. Tretiak, S. A. Crooker, C. Katan, M. G. Kanatzidis, J. J. Crochet, J. Even, A. D. Mohite, *Nat. Commun.* **2018**, *9*, 2254.
[15] M. Sidler, P. Back, O. Cotlet, A. Srivastava, T. Fink, M. Kroner, E. Demler, A. Imamoglu, *Nat. Phys.* **2017**, *13*, 255.
[16] M. M. Glazov, *J. Chem. Phys.* **2020**, *153*, 034703.
[17] M. A. Lampert, *Phys. Rev. Lett.* **1958**, *1*, 450.
[18] K. Kheng, R. Cox, M. d' Aubigné, F. Bassani, K. Saminadayar, S. Tatarenko, *Phys. Rev. Lett.* **1993**, *71*, 1752.
[19] D. Sanvitto, F. Pulizzi, A. J. Shields, P. C. M. Christianen, S. N. Holmes, M. Y. Simmons, D. A. Ritchie, J. C. Maan, M. Pepper, *Science* **2001**, *294*, 837.
[20] P. Soubelet, J. Klein, J. Wierzbowski, R. Silvioli, F. Sigger, A. V. Stier, K. Gallo, J. J. Finley, *Nano Lett.* **2021**, *21*, 959.
[21] G. Cheng, B. Li, Z. Jin, M. Zhang, J. Wang, *Nano Lett.* **2021**, *21*, 6314.
[22] V. Agranovich, D. Basko, K. Schmidt, G. LaRocca, F. Bassani, S. Forrest, K. Leo, D. Lidzey, *Chem. Phys.* **2001**, *272*, 159.
[23] Y. Cho, S. M. Greene, T. C. Berkelbach, *Phys. Rev. Lett.* **2021**, *126*, 216402.
[24] N. S. Makarov, S. Guo, O. Isaienko, W. Liu, I. Robel, V. I. Klimov, *Nano Lett.* **2016**, *16*, 2349.
[25] G. Rainò, G. Nedelcu, L. Protesescu, M. I. Bodnarchuk, M. V. Kovalenko, R. F. Mahrt, T. Stöferle, *ACS Nano* **2016**, *10*, 2485.
[26] S. Nakahara, H. Tahara, G. Yumoto, T. Kawawaki, M. Saruyama, R. Sato, T. Teranishi, Y. Kanemitsu, *J. Phys. Chem. C* **2018**, *122*, 22188.
[27] U. N. Huynh, Y. Liu, A. Chanana, D. R. Khanal, P. C. Sercel, J. Huang, Z. V. Vardeny, *Nat. Commun.* **2022**, *13*, 1428.
[28] M. Seitz, P. Gant, A. Castellanos-Gomez, F. Prins, *Nanomaterials* **2019**, *9*, 1120.
[29] J. D. Ziegler, J. Zipfel, B. Meisinger, M. Menahem, X. Zhu, T. Taniguchi, K. Watanabe, O. Yaffe, D. A. Egger, A. Chernikov, *Nano Lett.* **2020**, *20*, 6674.
[30] T. T. H. Do, A. Granados del Águila, D. Zhang, J. Xing, S. Liu, M. A. Prosnikov, W. Gao, K. Chang, P. C. M. Christianen, Q. Xiong, *Nano Lett.* **2020**, *20*, 5141.
[31] J. S. Ross, S. Wu, H. Yu, N. J. Ghimire, A. M. Jones, G. Aivazian, J. Yan, D. G. Mandrus, D. Xiao, W. Yao, X. Xu, *Nat. Commun.* **2013**, *4*, 1474.
[32] A. Esser, E. Runge, R. Zimmermann, W. Langbein, *Phys. Status Solidi A* **2000**, *178*, 489.

[33] K. F. Mak, K. He, C. Lee, G. H. Lee, J. Hone, T. F. Heinz, J. Shan, *Nat. Mater.* **2013**, *12*, 207.
[34] J. Zipfel, K. Wagner, M. A. Semina, J. D. Ziegler, T. Taniguchi, K. Watanabe, M. M. Glazov, A. Chernikov, *Phys. Rev. B* **2022**, *105*, 075311.
[35] K. Wagner, E. Wietek, J. D. Ziegler, M. A. Semina, T. Taniguchi, K. Watanabe, J. Zipfel, M. M. Glazov, A. Chernikov, *Phys. Rev. Lett.* **2020**, *125*, 267401.
[36] D. A. Egger, A. M. Rappe, L. Kronik, *Acc. Chem. Res.* **2016**, *49*, 573.
[37] X. Hong, T. Ishihara, A. Nurmikko, *Solid State Commun.* **1992**, *84*, 657.
[38] O. V. Mikhnenko, P. W. M. Blom, T.-Q. Nguyen, *J. Energy Environ. Sci.* **2015**, *8*, 1867.
[39] J. Erland, B. S. Razbirin, K.-H. Pantke, V. G. Lyssenko, J. M. Hvam, *Phys. Rev. B* **1993**, *47*, 3582.
[40] K. Wagner, J. Zipfel, R. Rosati, E. Wietek, J. D. Ziegler, S. Brem, R. Perea-Causín, T. Taniguchi, K. Watanabe, M. M. Glazov, E. Malic, A. Chernikov, *Phys. Rev. Lett.* **2021**, *127*, 076801.
[41] C. C. Stoumpos, D. H. Cao, D. J. Clark, J. Young, J. M. Rondinelli, J. I. Jang, J. T. Hupp, M. G. Kanatzidis, *Chem. Mater.* **2016**, *28*, 2852.
[42] W. Peng, J. Yin, K.-T. Ho, O. Ouellette, M. De Bastiani, B. Murali, O. El Tall, C. Shen, X. Miao, J. Pan, E. Alarousu, J.-H. He, B. S. Ooi, O. F. Mohammed, E. Sargent, O. M. Bakr, *Nano Lett.* **2017**, *17*, 4759.
[43] S.-Y. Chen, T. Goldstein, T. Taniguchi, K. Watanabe, J. Yan, *Nat. Commun.* **2018**, *9*, 3717.
[44] A. Castellanos-Gomez, M. Buscema, R. Molenaar, V. Singh, L. Janssen, H. S. J. van der Zant, G. A. Steele, *2D Mater.* **2014**, *1*, 011002.
[45] L. Wang, I. Meric, P. Y. Huang, Q. Gao, Y. Gao, H. Tran, T. Taniguchi, K. Watanabe, L. M. Campos, D. A. Muller, J. Guo, P. Kim, J. Hone, K. L. Shepard, C. R. Dean, *Science* **2013**, *342*, 614.
[46] M. Dyksik, H. Duim, X. Zhu, Z. Yang, M. Gen, Y. Kohama, S. Adjokatse, D. K. Maude, M. A. Loi, D. A. Egger, M. Baranowski, P. Plochocka, *ACS Energy Lett.* **2020**, *5*, 3609.
[47] S. Bubin, L. Adamowicz, *J. Chem. Phys.* **2006**, *124*, 224317.
[48] J. Mitroy, S. Bubin, W. Horiuchi, Y. Suzuki, L. Adamowicz, W. Cencek, K. Szalewicz, J. Komasa, D. Blume, K. Varga, *Rev. Mod. Phys.* **2013**, *85*, 693.